LETTER

Spontaneous emission of matter waves from a tunable open quantum system

Ludwig Krinner[1], Michael Stewart[1], Arturo Pazmiño[1], Joonhyuk Kwon[1] & Dominik Schneble[1]*

The decay of an excited atom undergoing spontaneous photon emission into the fluctuating quantum-electrodynamic vacuum is an emblematic example of the dynamics of an open quantum system. Recent experiments have demonstrated that the gapped photon dispersion in periodic structures, which prevents photons in certain frequency ranges from propagating, can give rise to unusual spontaneous-decay behaviour, including the formation of dissipative bound states[1–3]. So far, these effects have been restricted to the optical domain. Here we demonstrate similar behaviour in a system of artificial emitters, realized using ultracold atoms in an optical lattice, which decay by emitting matter-wave, rather than optical, radiation into free space. By controlling vacuum coupling and the excitation energy, we directly observe exponential and partly reversible non-Markovian dynamics and detect a tunable bound state that contains evanescent matter waves. Our system provides a flexible platform for simulating open-system quantum electrodynamics and for studying dissipative many-body physics with ultracold atoms[4–6].

The Weisskopf–Wigner model of spontaneous emission[7,8], a central concept in quantum optics[9], describes how an excited atom can decay to its ground state owing to coupling to zero-point oscillations of the electromagnetic vacuum. It simultaneously represents one of the first open quantum systems discussed in the literature and an area of research that has recently seen a resurgence of intense theoretical efforts[10–13]. In its usual Markovian formulation, the model makes the assumption that the decay proceeds on a much slower timescale than the optical period, which leads to a memoryless, exponential decay of the excited-state amplitude and to an associated Lamb shift of the transition frequency. For free-space emission, the Markovian approximation is generally fulfilled to high accuracy.

On the other hand, modifications to the mode density of the vacuum can change the features of spontaneous decay. This was recognized first in the 1940s[14] and again decades later[15], during the development of cavity quantum electrodynamics[16–18], where the decay can be altered to the extreme point of coherent vacuum Rabi oscillations when the spectrum is restricted to a single mode. Between these two limits lies the regime of a vacuum with a bounded continuous spectrum, in which a strong modification of spontaneous decay behaviour occurs close to the boundary. An example is photonic crystals (also called photonic-bandgap materials)[19,20], where a periodic spatial modulation of the refractive index gives rise to a gapped dispersion relation. For emission close to a bandgap, the Markovian approximation can no longer be applied, and novel features appear, including oscillatory decay dynamics for energies above the band edge and the formation of atom–photon bound states below it[21]. Over the past two decades, experiments on spontaneous emission in photonic-bandgap materials, including the microwave domain, have observed some of these effects, specifically modified spontaneous emission rates[22,23] and Lamb shifts[24], as well as spectral signatures for non-exponential decay[1]. Very recently, experiments have probed the long-predicted atom–photon bound state[25,26], using both transmon qubits coupled to corrugated microwave guides[3] and atoms in photonic-crystal waveguides[2],

with the prospect of engineering systems with optical long-range interactions[27].

Here, we realize an atom–optical analogue[4–6] of emission in a one-dimensional photonic-bandgap material, where the singularity in the mode density near the edge of the continuum leads to particularly strong deviations from Markovian behaviour. In our system of matter-wave emitters, the free tunability of the excitation energy and decay strength allows for a systematic exploration of the emergence of non-Markovian dynamics, including partial reversibility and the formation of a matter-wave bound state that can be directly detected. Importantly, the close spacing of emitters gives rise to collectively enhanced dynamics beyond the Weisskopf–Wigner model.

The experimental configuration is shown in Fig. 1a. Using a deep three-dimensional optical lattice with state selectivity along one axis, we prepare a sparse array of atoms confined to sites that are embedded in a system of isolated tubes acting as one-dimensional waveguides (see Methods for details). An atom's internal state ($|r\rangle$, red) is coherently coupled to a second, unconfined internal state ($|b\rangle$, blue) using an oscillatory magnetic field. Each site thus acts as a two-level matter-wave emitter, with harmonic-oscillator ground-state occupational levels $|g\rangle$ (empty) and $|e\rangle$ (full), supporting both the emission (for $|e\rangle \rightarrow |g\rangle$) and the absorption (for $|g\rangle \rightarrow |e\rangle$) of a $|b\rangle$ atom. The excitation energy of the emitter, which is given by the detuning, Δ, of the coherent coupling from the atomic resonance, is converted into kinetic energy for atomic motion along the axis of the waveguide.

One of the main features of each matter-wave emitter is its ability to undergo spontaneous decay, as described by the Weisskopf–Wigner model. Assuming no lattice potential, the driven atom performs simple Rabi oscillations between two internal states $|r\rangle$ and $|b\rangle$. These oscillations are described by the Hamiltonian $\hat{H} = (\hbar\Omega/2)e^{i\delta t}\hat{r}\hat{b}^{\dagger} + \text{h.c.}$, where Ω denotes the strength and δ the detuning of the coupling from the bare atomic resonance, $\hbar$ is the Planck constant and 'h.c.' denotes the Hermitian conjugate. The tight confinement of just one of the states (here, $|r\rangle$) strongly couples the atom's internal and motional degrees of freedom, producing a zero-point energy shift of $\bar{\varepsilon}_0 = \hbar\omega_0/2 \gg \hbar\Omega$, where ω_0 is the harmonic-oscillator frequency in the potential, as well as a kinetic-energy shift of $\varepsilon_k = \hbar^2 k^2/(2m)$ for the motion of the free $|b\rangle$ state at $\hbar k$ momentum. As a consequence, the detuning and strength of the coupling are shifted to $\Delta_k = \delta + (\bar{\varepsilon}_0 - \varepsilon_k)/\hbar$ and $\Omega_k = \Omega\gamma_k$, respectively, with $\gamma_k = \langle k|\psi_e\rangle$ denoting the overlap of the external wavefunctions. Integration over all possible momenta k then yields[6] $\hat{H} = \sum_k \hbar g_k e^{i\Delta_k t}|g\rangle\langle e|\hat{b}_k^{\dagger} + \text{h.c.}$, with $g_k = \Omega_k/2$; that is, the standard Weisskopf–Wigner Hamiltonian describing spontaneous emission into a vacuum of modes (k, ε_k) (see Fig. 1b). In contrast to optical emission in free space, the dispersion relation ε_k is quadratic, as in a photonic crystal (see Fig. 1c). In such crystals, the emission energy relative to the edge of the continuum may be adjusted through the crystal's band structure; in our system, the excitation energy, $\hbar\Delta \equiv \hbar\Delta_{k=0}$, itself is tunable, including the case $\Delta < 0$. Importantly, the tunability also includes the vacuum coupling, g_k, which is set by Ω.

A common scenario considered in the Wigner–Weisskopf model is emission deep into the continuum, such that the decay dynamics is

[1]Department of Physics and Astronomy, Stony Brook University, Stony Brook, NY, USA. *e-mail: dominik.schneble@stonybrook.edu
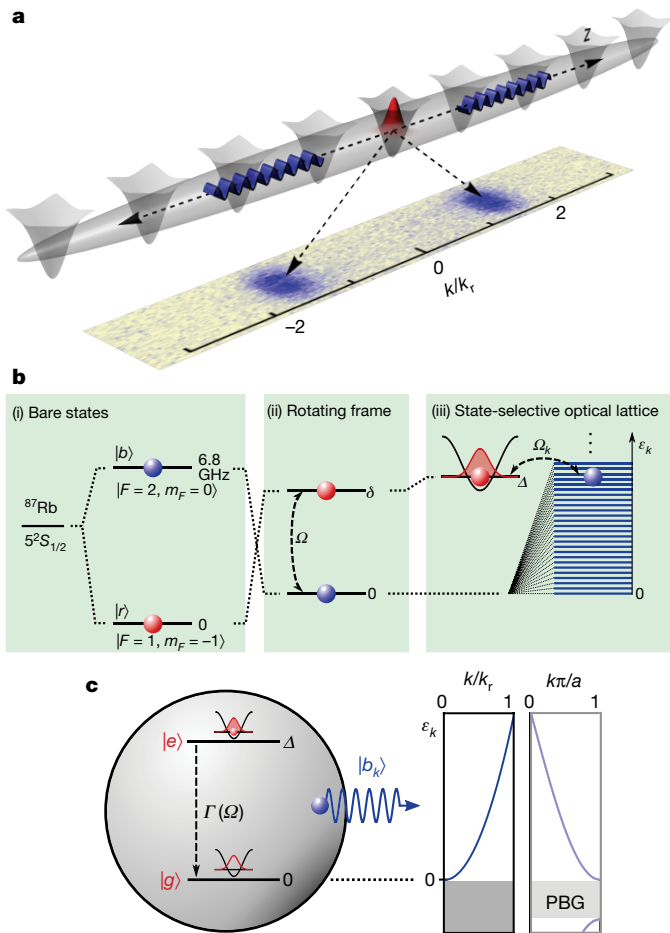
Fig. 1 | Realization of matter-wave emitters. a, Experimental configuration. An occupied site of an optical lattice embedded in a single-mode matter waveguide acts as an elementary emitter of a single atom; adjacent empty lattice sites act as absorbers. The bottom illustration shows the momentum distribution in the waveguide after release and free expansion, where $\hbar k_r = \hbar(2\pi/\lambda_z)$ (with a wavelength of $\lambda_z = 790.1$ nm) is the recoil momentum. **b**, Emission mechanism: (i) bare internal-state pair in ^{87}Rb (hyperfine ground states $|r\rangle = |F = 1, m_F = -1\rangle$ and $|b\rangle = |F = 2, m_F = 0\rangle$ split by 6.8 GHz); (ii) state pair in a frame co-rotating with a near-resonant microwave field with variable detuning δ and coupling strength Ω; and (iii) state pair in the co-rotating frame after applying the state-selective lattice potential (detuning shifted to $\Delta = \delta + \omega_0/2$, where $\omega_0 = h \times 40$ kHz). The microwave couples (with $\Omega_k = \Omega\gamma_k$) the trapped $|r\rangle$ state to free $|b_k\rangle$ states with momentum k and kinetic energy ε_k. **c**, The filled (empty) potential well can be viewed as the excited (ground) state $|e\rangle$ ($|g\rangle$) of a matter-wave emitter. The emission of atoms in this scenario is similar to the emission of photons in photonic-bandgap (PBG) materials, with both featuring quadratic dispersions and energetically forbidden regions.

Fig. 2 | Markovian regime. a, Time evolution of the lattice population for $\Omega = 2\pi \times 0.74(5)$ kHz and $\Delta = 2\pi \times 1.9(3)$ kHz (red symbols). Each point is the average of at least three measurements and error bars show the standard error of the mean (s.e.m.). The red line is a phenomenological exponential decay curve with a fitted rate of $2\pi \times 94(3)$ Hz and an offset of 0.503(4). The light-grey lines represent the Markovian approximation (dashed, $\Gamma = 2\pi \times 72(12)$ Hz) and the exact analytical solution for an isolated emitter[6] (solid). **b**, Lattice population as a function of Δ for $t = 0.4$ ms and $\Omega = 2\pi \times 1.5(1)$ kHz. The solid line is the Markovian expectation with the overall decay width, Γ, scaled by 0.61(1). **c**, Detected momentum distribution of $|b\rangle$ atoms versus Δ for parameters as in **b**. The dashed line is the single-particle dispersion; data for small positive and for negative detunings are outside the Markovian regime. **d**, Raw time-of-flight data for extracting the energy shift at $\Delta = 2\pi \times 6.0(3)$ kHz. Colour scale as in **c**. **e**, Measured shifts $\bar\delta_L = \Delta_{\bar k} - \Delta$ in the regime $\Omega/\Delta < 1$ for $\bar\Omega t = 1.24$ and averaged over $\Delta = 2\pi \times \{1, 2, 4, 6\}$ kHz. The data are extracted from the second moment (maximum) of the momentum distribution, shown by blue squares (red circles). Error bars show the s.e.m. The blue solid and red dashed lines are quadratic fits and the grey dotted line represents $\delta_L(\Omega)$.

much slower than the timescale set by the excited-state energy (or the elevation above the band edge in the case of a photonic crystal). This allows for a Markovian treatment and results in exponential decay of the excited state. Following Fermi's golden rule, the decay width, Γ, is the product of the mode density, ρ, and the square of a matrix element, H_{ge}, which for optical decay is the product of the electric dipole moment and the zero-point field of the resonant mode. For our system, an analogous analysis[6] (valid for $\Omega/\Delta \ll 1$) leads to $\Gamma = \Omega_{\bar k}^2 / \sqrt{\omega_0 \Delta}$, containing the one-dimensional mode density $\rho \propto 1/\sqrt{\Delta}$ and $H_{ge} \propto \hbar\Omega_{\bar k}$, where $\bar k = \sqrt{2m\Delta/\hbar}$ represents the resonant mode.

Because of the residual axial tube confinement, ω_z, all measurements are taken for $\Omega/\omega_z > 1$ and associated timescales shorter than $\tau_z = 2\pi/\omega_z \approx 10$ ms. The measured $|r\rangle$ population is shown in Fig. 2 for parameters in the (quasi-)Markovian regime $(\Omega/\Delta)^2 \ll 1$ as a function
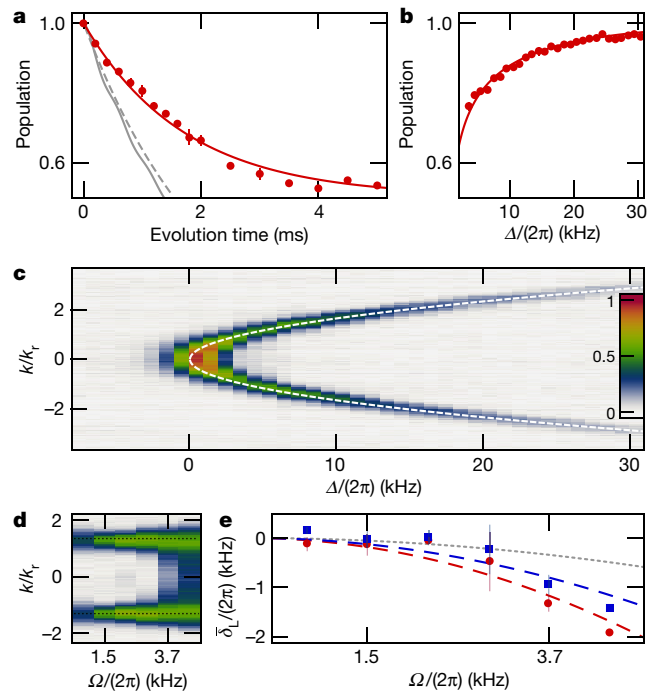
of time (Fig. 2a) and detuning (Fig. 2b); the data in Fig. 2a are for $\Omega/\Delta \approx 0.4$ at $\Delta \approx 2\pi \times 2$ kHz (with $\Gamma = 2\pi \times 72$ Hz). After a variable coupling time t, we observe an irreversible, exponential decay in agreement with the expectation; however, the measured population does not decay to zero but instead saturates at a finite value. We qualitatively explain this discrepancy by taking into account that an excited emitter is not isolated but part of a (mostly) ground-state array that enables reabsorption, in analogy to an optically thick medium. In the Weisskopf–Wigner formalism, the array is modelled by introducing site-dependent phases and projectors, resulting in[4] $\hat{H} = \sum_{k,j} \hbar g_k e^{i(\Delta_k t - kz_j)} |g_j\rangle\langle e_j| \hat{b}_k^\dagger + \text{h.c.}$ Following a master-equation-based treatment[5], we expect excitations to be transferred between neighbours on a timescale of $t \approx 1/\Gamma = 2$ ms, leading to a slowdown of the decay, in qualitative agreement with Fig. 2a (see also Methods section 'Numerical simulation of array effects'). Moreover, the emitted atoms cannot escape from our system for long times, which induces the formation of a steady state as t approaches τ_z. Here, additional dephasing effects that are not considered in this model may arise from collisions between emitted atoms (scattering between modes in each tube). At early times, $t < 1/\Gamma$, with still weak reabsorption, the decay at a fixed time τ (see Fig. 2b) displays approximately the expected detuning dependence of the Weisskopf–Wigner model, $\exp[-\Gamma(\Delta)\tau] \approx 1 - \Gamma(\Delta)\tau$ (albeit with a downward
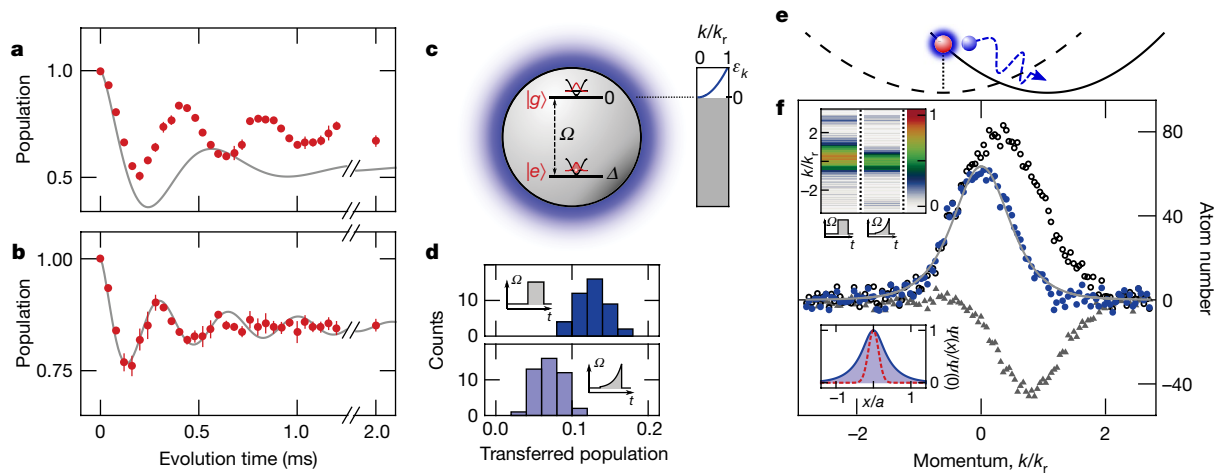
Fig. 3 | Non-Markovian dynamics and bound-state formation.
a, Time evolution of the $|r\rangle$ population for $\Delta = -2\pi \times 0.1(3)$ kHz and $\Omega = 2\pi \times 3.0(3)$ kHz (with points and error bars as in Fig. 2a). The grey line is our analytical model. **b**, Same as **a**, but for $\Delta = -2\pi \times 1.7(3)$ kHz. The fitting parameters of the analytical model are $\Delta = -2\pi \times 2.08(3)$ kHz and $\Omega = 2\pi \times 2.79(4)$ kHz. **c**, Illustration of a stationary bound state for negative excitation energies. **d**, Asymptotic fraction of $|b\rangle$ atoms, extracted from the time evolution after $t = 2.6$ ms, for Ω as in **a** and $\Delta = -2\pi \times 2.2(3)$ kHz. The top (bottom) histogram refers to the case of a sudden (adiabatic) turn-on of the coupling, measured from 50 experimental runs each. **e**, Illustration of separation of evanescent and propagating waves along the weakly confining tube axis. The atomic sample resides off-centre from the minimum of the axial tube potential (solid line), shifted from that of the initial trap (dashed line), which defines the sample position. While the sample and bound state are frozen

in place (vertical dotted line), the nonadiabatically released fraction (blue arrow) is accelerated towards the potential minimum. **f**, Momentum distributions of $|b\rangle$ atoms for the two scenarios considered in **d**. Open (filled) circles represent the sudden (adiabatic) turn-on of the coupling, averaged over all 50 runs, and triangles show the difference of the two datasets. The solid line represents the square of the Fourier transform of the analytical evanescent wavefunction[6], fitted to the adiabatic data ($\Delta_{\mathrm{fit}} = 2\pi \times 2.1(1)$ kHz). The centre of mass of the non-adiabatic dataset is shifted by $p_s = 0.32(1)\hbar k_r$ relative to the adiabatic dataset, and that of their difference (with a half-width at half-maximum of $0.57(1)\hbar k_r$) is shifted by $p_s = 0.80(1)\hbar k_r$. The expectation for free atoms is $p_s = 0.83(7)\hbar k_r$. Lower inset, corresponding real-space evanescent wavefunction (blue, solid) and Wannier function of a lattice-trapped $|r\rangle$ atom (dashed, red). Upper inset, raw data for the momentum distributions of **e**, before subtraction of spurious higher-band contributions (see Methods).

rescaling of the actual value of Γ at the finite pulse time $\tau = 0.4$ ms used, with reabsorption effects already apparent).

We next characterize the momentum distribution of the emitted atoms. For this purpose we apply a 0.4-ms-long coupling pulse and then observe the location of the $|b\rangle$ atoms after 15 ms of free fall, using state-selective absorptive imaging (see Methods). On the basis of the Markovian approximation, isotropic emission with wavepackets centred near the resonant momentum $\bar{k}(\Delta)$ is expected. In Fig. 2c we show the observed momentum distribution as a function of Δ; the emission clearly exhibits parabolic dispersion. Moreover, the spectral width, σ_k, of the separated wavepackets decreases with detuning, in qualitative agreement with the expectation ($\sigma_k \propto 1/\Delta$ for large detunings[6]; a quantitative comparison is compromised by the finite time of flight). The 'intensity' of the emitted matter-wave pulse strongly depends on the detuning, as shown in Fig. 2b.

The standard Markovian treatment of the Weisskopf–Wigner model yields a Lamb shift of the ground and excited states as a unitary coupling to the vacuum. An analogous analysis for our system[4,6] yields a shift $\delta_L = \Omega^2/\omega_0$ of the excited-state energy, to ($\Delta - \delta_L$). We measure the momentum distribution for variable Ω at several values of Δ and then calculate the mean kinetic energy of the wavepackets both from the second moment of the momentum distributions and from the location of their fitted maxima (see Methods for details). To facilitate comparison with the model, the data are taken for a constant effective pulse area $\tilde{\Omega}t$, where $\tilde{\Omega} = (\Omega/\omega_0)^{1/3}\Omega$, and $t \leq 1$ ms to mitigate propagation effects. The results for the (quasi-)Markovian regime $(\Omega/\Delta)^2 \ll 1$ are shown in Fig. 2d, e as a function of Ω. The extracted shift has the sign and approximate quadratic dependence of δ_L but is a factor of roughly three larger. We caution that while this alone could point towards the existence of collective enhancement, there is no indication for super-radiance[4,28] from the decay data (which is consistent with the fact that there is no overall population inversion in the array).

Our system readily allows the study of spontaneous emission outside the Markovian regime, as shown in Fig. 2c. In particular, the diverging one-dimensional mode density near $\varepsilon_k = 0$ greatly enhances the effects of the edge of the continuum. For emission at low excitation energy, for

$\Delta/\Omega \ll 1$, we expect dynamics reminiscent of a two-level system, with damping provided by low-energy modes. Results of measurements at $\Delta = 0$ are shown in Fig. 3a. We observe oscillations similar to the predictions of our isolated-emitter model[6] (which now features a finite offset, in contrast to positive detunings) but with higher frequency and less damping, suggesting that the dynamics is coherently enhanced by low-energy modes whose wavelengths can extend over several emitters (see also Methods section 'Numerical simulation of array effects').

For emission below the continuum edge (that is, for $\Delta < 0$), we expect the formation of a stationary bound state[4,6], as illustrated in Fig. 3c. For our one-dimensional system, this state consists of a partly excited emitter dressed by an evanescent, approximately exponentially decaying matter wave, with a binding energy of $\hbar\omega_B \approx \hbar\Delta$ and a localization length[6] of $\xi = 1/\sqrt{2m|\omega_B|/\hbar}$. To isolate the bound state, the coupling needs to be turned on slowly to prevent the additional population of freely propagating modes[6] representing a non-adiabatic, transient shedding of matter waves. However, first we proceed as before by switching on the coupling, at $\Delta = -2\pi \times 1.7$ kHz. The lattice population, shown in Fig. 3b, shows a transient oscillation (with much lower amplitude than at the edge) settling to an asymptotic value below unity (with an observable $|b\rangle$ population; see Fig. 2c). Remarkably, our isolated-emitter model[6] now closely fits the data within the experimental uncertainties. Indeed, for the chosen parameters, ξ is less than half a lattice period, which should lead to a relative suppression of long-range couplings.

To access the properties of the bound state, we first determine the fraction of $|b\rangle$ atoms by comparing the asymptotic lattice population for a sudden and for an exponential turn-on of the coupling. The results in Fig. 3d show that 7.1(2)% of the population are in the evanescent wave, with a total $|b\rangle$ population of 12.7(2)% (here and elsewhere the errors quoted denote one standard deviation). The observed fraction of $|b\rangle$ atoms in the bound state (55%) is close to the expectation[6] of 47% for the chosen parameters, with the excess possibly stemming from residual non-adiabaticity of the ramping (we noticed an inconsistency in ref. [6] for the total $|b\rangle$ fraction, but this does not affect the relative $|b\rangle$ fraction in the bound state). Importantly, the recorded momentum distribution of

the bound evanescent fraction of $|b\rangle$ atoms (see Fig. 3f) can be directly compared to the prediction of our analytical model[6] owing to the absence of propagation effects. Fitting the model to the data for the adiabatic ramp-up with Δ as the only fitting parameter reproduces its experimental value to within the experimental uncertainty, and the agreement between the model and the measured momentum distribution is indeed excellent. The localization length obtained from the exact model is $\xi = 142(3)$ nm (we note that for the parameters chosen[6], $\omega_B \approx 1.3\Delta$).

Finally, additional direct evidence for the non-adiabatically released part can be obtained by comparing the adiabatic momentum distribution to that recorded after the rectangular pulse. Because our sample is prepared off-centre from the potential minimum along the tube direction (see Fig. 3e, Methods), the distribution of the shed $|b\rangle$ atoms can separate in momentum space from the bound fraction. The pulse duration used in this experiment corresponds to about a quarter of the oscillation period (2.6 ms) along the tube axis, thus maximizing this differential effect. As seen in Fig. 3f, the (symmetric) difference of the two momentum distributions is centred at the finite momentum expected for atoms released with zero velocity at the beginning of the pulse. This finding is consistent with the time evolution in Fig. 3b, which suggests that the release of the unbound fraction occurs within a short time (about 0.5 ms) after the coupling is turned on. We note that as a result of propagation in the tubes for a quarter of the oscillation period, the width of the momentum distribution of the released atoms reflects that of their distribution in real space ($v_z = z\omega_z$). The extracted half-width at half-maximum of 5.47(9) μm is comparable to the Thomas–Fermi radius of the initial condensate.

Much of the present work has focused on basic properties arising from the tunability of our Wigner–Weisskopf system, including the formation of bound states below the edge of the mode continuum. On the single-emitter level, this provides a direct analogy to atomic decay near the bandgap of a photonic crystal. We note that in yet another context, the observed non-Markovian oscillatory dynamics also reproduces predictions for electron photodetachment from negative ions[29,30]. The optical lattice geometry opens up various additional avenues of inquiry. For emission sufficiently above the continuum edge, these may include novel types of superradiance that depend on the degree of coherence of the lattice population (superfluid or Mott insulating)[4,5] and have no analogue in optical systems. Moreover, controlling the longitudinal waveguide level spacing should enable studies of the transition between Dicke- and Tavis–Cummings-type models in quantum optics[4,9] (restricted to co-rotating terms), including their modification in the non-Markovian regime. Unlike photons, the emitted atoms can directly interact with each other, which should give rise to additional, nonlinear effects that modify the population dynamics. For negative energies, the bound state lends itself to the realization of lattice models[4] with modified tunnelling and interactions. Superficially, the structure of the bound state resembles that of a lattice polaron[31,32] (for which a phononic Lamb shift has recently been measured[33]), with massive vacuum excitations replacing massless Bogoliubov sound excitations. Rather than reducing transport, the bound state here leads to an enhancement of mobility. The presence of tunnelling with a tunable range is of interest, for example, for studies of integrability and thermalization in one-dimensional geometries.

Online content

Any Methods, including any statements of data availability and Nature Research reporting summaries, along with any additional references and Source Data files, are available in the online version of the paper at https://doi.org/10.1038/s41586-018-0348-z.

1. Hoeppe, U. et al. Direct observation of non-Markovian radiation dynamics in 3D bulk photonic crystals. *Phys. Rev. Lett.* **108**, 043603 (2012).
2. Hood, J. D. et al. Atom–atom interactions around the band edge of a photonic crystal waveguide. *Proc. Natl Acad. Sci. USA* **113**, 10507–10512 (2016).
3. Liu, Y. & Houck, A. A. Quantum electrodynamics near a photonic bandgap. *Nat. Phys.* **13**, 48–52 (2017).
4. de Vega, I., Porras, D. & Cirac, J. I. Matter-wave emission in optical lattices: single particle and collective effects. *Phys. Rev. Lett.* **101**, 260404 (2008).
5. Navarrete-Benlloch, C., de Vega, I., Porras, D. & Cirac, J. I. Simulating quantum-optical phenomena with cold atoms in optical lattices. *New J. Phys.* **13**, 023024 (2011).
6. Stewart, M., Krinner, L., Pazmiño, A. & Schneble, D. Analysis of non-Markovian coupling of a lattice-trapped atom to free space. *Phys. Rev. A* **95**, 013626 (2017).
7. Weisskopf, V. & Wigner, E. Berechnung der natürlichen Linienbreite auf Grund der Diracschen Lichttheorie. *Z. Phys.* **63**, 54–73 (1930).
8. Milonni, P. W. *The Quantum Vacuum: An Introduction to Quantum Electrodynamics* (Academic Press, San Diego, 1994).
9. Meystre, P. & Sargent, M. III *Elements of Quantum Optics* (Springer, Berlin, 2007).
10. Rivas, A., Huelga, S. F. & Plenio, M. B. Quantum non-Markovianity: characterization, quantification and detection. *Rep. Prog. Phys.* **77**, 094001 (2014).
11. Rotter, I. & Bird, J. P. A review of progress in the physics of open quantum systems: theory and experiment. *Rep. Prog. Phys.* **78**, 114001 (2015).
12. Breuer, H.-P., Laine, E.-M., Piilo, J. & Vacchini, B. Non-Markovian dynamics in open quantum systems. *Rev. Mod. Phys.* **88**, 021002 (2016).
13. de Vega, I. & Alonso, D. Dynamics of non-Markovian open quantum systems. *Rev. Mod. Phys.* **89**, 015001 (2017).
14. Purcell, E. M. Spontaneous emission probabilities at radio frequencies. *Phys. Rev.* **69**, 681 (1946).
15. Kleppner, D. Inhibited spontaneous emission. *Phys. Rev. Lett.* **47**, 233–236 (1981).
16. Miller, R. et al. Trapped atoms in cavity QED: coupling quantized light and matter. *J. Phys. B* **38**, S551–S565 (2005).
17. Walther, H., Varcoe, B. T. H., Englert, B.-G. & Becker, T. Cavity quantum electrodynamics. *Rep. Prog. Phys.* **69**, 1325–1382 (2006).
18. Haroche, S. & Raimond, J.-M. *Exploring the Quantum: Atoms, Cavities, and Photons* (Oxford Univ. Press, Oxford, 2006).
19. John, S. Strong localization of photons in certain disordered dielectric superlattices. *Phys. Rev. Lett.* **58**, 2486–2489 (1987).
20. Yablonovitch, E. Inhibited spontaneous emission in solid-state physics and electronics. *Phys. Rev. Lett.* **58**, 2059–2062 (1987).
21. Lambropoulos, P., Nikolopoulos, G. M., Nielsen, T. R. & Bay, S. Fundamental quantum optics in structured reservoirs. *Rep. Prog. Phys.* **63**, 455–503 (2000).
22. Tocci, M. D., Scalora, M., Bloemer, M. J., Dowling, J. P. & Bowden, C. M. Measurement of spontaneous-emission enhancement near the one-dimensional photonic band edge of semiconductor heterostructures. *Phys. Rev. A* **53**, 2799–2803 (1996).
23. Lodahl, P. et al. Controlling the dynamics of spontaneous emission from quantum dots by photonic crystals. *Nature* **430**, 654–657 (2004).
24. Liu, Q. et al. Observation of Lamb shift and modified spontaneous emission dynamics in the YBO$_3$: Eu^{3+} inverse opal. *Opt. Lett.* **35**, 2898–2900 (2010).
25. Bykov, V. P. Spontaneous emission from a medium with a band spectrum. *Sov. J. Quantum Electron.* **4**, 861–871 (1975).
26. John, S. & Wang, J. Quantum electrodynamics near a photonic band gap: photon bound states and dressed atoms. *Phys. Rev. Lett.* **64**, 2418–2421 (1990).
27. Douglas, J. S., Habibian, H., Hung, C.-L., Gorshkov, A. V., Kimble, H. J. & Chang, D. E. Quantum many-body models with cold atoms coupled to photonic crystals. *Nat. Photon.* **9**, 326–331 (2015).
28. Dicke, R. H. Coherence in spontaneous radiation processes. *Phys. Rev.* **93**, 99–110 (1954).
29. Rzążerewski, K., Lewenstein, M. & Eberly, J. H. Threshold effects in strong-field photodetachment. *J. Phys. B* **15**, L661–L667 (1982).
30. Lewenstein, M. & Rzążewski, K. Quantum anti-Zeno effect. *Phys. Rev. A* **61**, 022105 (2000).
31. Bruderer, M., Klein, A. Clark, S. R. & Jaksch, D. Polaron physics in optical lattices. *Phys. Rev. A* **76**, 011605, 2007.
32. Gadway, B., Pertot, D., Reimann, R. & Schneble, D. Superfluidity of interacting bosonic mixtures in optical lattices. *Phys. Rev. Lett.* **105**, 045303 (2010).
33. Rentrop, T. et al. Observation of the phononic Lamb shift with a synthetic vacuum. *Phys. Rev. X* **6**, 041041 (2016).

Author contributions D.S., L.K. and M.S. conceived the experiment. L.K. took the measurements with assistance from A.P. and J.K. L.K. analysed the data with contributions from M.S. Numerical simulations were performed by L.K. D.S. supervised the project. The results were discussed and interpreted by all authors. The manuscript was written by L.K. and D.S. with contributions from A.P., J.K. and M.S.

METHODS

Experimental procedures. In this section we outline experimental procedures implemented in our measurements.

Sample preparation. In the experiment we used [87]Rb atoms in the hyperfine ground states $|r\rangle = |F = 1, m_F = -1\rangle$ and $|b\rangle = |2, 0\rangle$ (the fact that $|r\rangle$ lies below $|b\rangle$ is inconsequential in the rotating frame). The atoms are confined to a two-dimensional array of roughly 10^3 isolated lattice tubes spaced at 532 nm, each with a radial confinement of $\omega_\perp = 2\pi \times 26$ kHz and a residual axial confinement of $\omega_z = 2\pi \times 97$ Hz that quantizes the mode spectrum for released $|b\rangle$ atoms in the z direction; this confinement is inconsequential for times much shorter than $\tau_z = 2\pi/\omega_z \approx 10$ ms. A state-selective lattice with period $\lambda_z/2 = 395$ nm and harmonic-oscillator frequency $\omega_0 = 2\pi \times 40(1)$ kHz strongly confines the $|r\rangle$ atoms along the tube axis.

Starting with an optically trapped Bose–Einstein condensate[34], we first create an atomic Mott insulator of $|r\rangle$ atoms by simultaneously ramping up all three optical lattices over a time of 90 ms to depths of $40E_{r,1,064nm}, 40E_{r,1,064nm}$ and $30E_{r,790.1nm}$, where $E_{r,\lambda} = (h/\lambda)^2/(2m)$ is the respective recoil energy, in the x, y and z directions, respectively. This procedure results in a deeply confined Mott-insulating sample, while also shifting the minimum of the tube potentials by about 10 μm with respect to the sample. The shift (which is comparable to the sample size and corresponds to the change of the gravitational sag during the ramp[34] after the atoms are effectively pinned by the z lattice) leaves the resonance condition for individual atoms unaffected because $|r\rangle$ and $|b\rangle$ experience the same tube potential.

After loading the atoms into the lattice, we transfer a fraction of approximately 0.82 to an intermediate state $|2, 1\rangle$ using a two-photon radiofrequency pulse (microwave radiation of 6.8 GHz and radiofrequency radiation of about 3 MHz) of 0.95 ms duration. These atoms are eventually removed using resonant light on the D2 cycling transition ($F = 2 \rightarrow F' = 3$). Using the $|2, 1\rangle$ state has the advantage that there is no first-order shift in the energy difference between $|1, -1\rangle$ and $|2, 1\rangle$ due to either magnetic field or the state-selective optical potential. Also, collisional shifts[35] of doubly (triply) occupied sites are roughly 50 Hz (100 Hz) for our lattice parameters, much less than the spectral width of the pulse. This yields a sample of $2.8(2) \times 10^4$ $|r\rangle$ atoms with an average site occupation of $\langle n_i\rangle \lesssim 0.5$ in the tubes. Having thus created an initial state of matter-wave emitters, we then switch on a 6.8-GHz microwave field of variable coupling strength Ω and detuning Δ.

Atom detection. We switch off the microwave coupling Ω suddenly, and we measure the population remaining in the lattice and access the momentum distribution of the released atoms with state-selective absorptive imaging, using a combination of band mapping and Stern–Gerlach separation during the time of flight (TOF).

The state detection begins with a 500-μs bandmap step during which all lattice potentials are ramped down to zero (the bandmap step prevents a rapid transverse expansion out of the tube potentials and is therefore favourable for momentum-space detection when small atom numbers are used). Subsequently all remaining trapping potentials are turned off suddenly, and after an expansion time of about 1 ms a pulse sequence is applied for magnetic-field characterization (see below), immediately followed by a 5-ms-long magnetic field gradient pulse to separate states of different magnetic moments. Finally, 14.5 ms after the release from the optical potential, a 200-μs-long imaging pulse of resonant light on the $F = 2 \rightarrow F' = 3$ D2 cycling transition is used to detect the $F = 2$ atoms; this yields a total effective TOF of 14.6 ms for atoms in this state. The $F = 1$ atoms are repumped for 100 μs using resonant D2 light ($F = 1 \rightarrow F' = 2$) after an additional 2.7 ms, immediately followed by another 200-μs-long imaging pulse (D2, $F = 2 \rightarrow F' = 3$) to detect the repumped $F = 1$ atoms after a total TOF of 17.6 ms. Because all magnetic moments are unique within $F = 1$ and $F = 2$ separately, we fully resolve the population in each individual hyperfine state $|F, m_F\rangle$. We note that technically the cloud centres of $F = 1$ and $F = 2$ along the imaging direction are still overlapped during the second imaging pulse, however the $F = 2$ atoms are pushed out of the field of view by the time the $F = 1$ detection occurs.

Image analysis. Our raw data are images acquired using a Princeton Instruments PIXIS:1024B charge-coupled device (CCD) camera with WinView32 software in .spe format. We use Mathematica to read the raw image data and create standard absorption images. Residual fringes are removed by subtracting typical fringes found using principal-component analysis of a large set (>100) of empty absorption images.

Momentum-space calibration. Our standard momentum calibration relies on Kapitza–Dirac diffraction[36] from the z lattice. For a more precise determination of emission momenta, we take into account residual propagation in the tubes that slows the atomic motion. After ramping up the z lattice, the tubes are created by partial retro-reflection of the Gaussian beams of our optical trap ($1/e^2$ radius of $w = 135$ μm)[34], which leads to an increase of the optical confinement $\omega_z/(2\pi)$ from 72(1) Hz to 97(1) Hz (with the gravity direction along z). The tubes are again ramped down within 500 μs after the microwave pulse (together with the z lattice, for band-mapping purposes), followed by a switch-off of the optical trap. We numerically simulate the motion of atoms in the tubes by assuming that the release (with momentum $\pm \bar{k}$) occurs midway through the pulse, at the centre of the 72-Hz

trap, and by calculating the trajectories in the time-dependent optical potential until detection, after a TOF of 14.6 ms. We see that the calibration differs from the Kapitza–Dirac diffraction results by −0.5%, −1% and −6% for pulse durations of 0.2 ms, 0.4 ms and 1 ms, respectively, with negligible differences for shorter pulses. These corrections are included in Fig. 2.

Characterization of magnetic fields and optical potentials. The quoted uncertainty of 300 Hz in the detuning Δ has contributions from both differential Zeeman and alternating-current Stark shifts, which are characterized as follows.

Magnetic fields. All experiments are carried out at fields between 4.9998(1) G and 5.0002(1) G, where the error corresponds to an uncertainty in the bare-level splitting of 70 Hz between $|r\rangle$ and $|b\rangle$. The magnetic field for each iteration of the experiment is monitored using a series of Rabi pulses during the TOF[37], in which atoms in $|1, -1\rangle$ are redistributed to the $|2, -2\rangle$ and $|2, -1\rangle$ states. This method allows field reconstruction to within 100 μG (for details see ref. [37]). The inhomogeneity of the magnetic field across the sample is characterized using a Ramsey pulse sequence. This inhomogeneity does not exceed 70 μG, which corresponds to a root-mean-square (r.m.s.) variation of Δ of 15 Hz across the sample for the ($|r\rangle$, $|b\rangle$) state pair.

Differential optical potential. The state-selective optical potential is created using a σ^--polarized laser beam (waist, 230 μm) at $\lambda_z = 790.10(2)$ nm. The polarization and wavelength are set (using a $\lambda/4$ waveplate and laser controls) such that the lattice potential seen by the $|r\rangle$ atoms is maximized, while the $|b\rangle$ atoms experience zero potential. The change in lattice potential with wavelength is $0.12E_r/(0.01$ nm), whereas the maximum theoretically possible polarization change (σ^- to π) changes the potential by $0.01E_r$ (we note that the polarization is stable in the experiment). We characterize the state selectivity using a sequence of ten Kapitza–Dirac pulses (10 μs) spaced at the Talbot resonance time[38], $\tau = (4E_{r,790.1nm}/h)^{-1} = 68$ μs, to ensure a suppression of the optical potential for $|b\rangle$ atoms by a factor of more than 100 with respect to that for $|r\rangle$ atoms, consistent also with the remaining wavelength uncertainty of 0.02 nm.

A crucial part of the experiment is the reliable determination of the resonance condition, or the value of Δ. Because the creation of our matter-wave emitter (Fig. 1c) starts with a detuned Rabi oscillation of two hyperfine states, we first (post-)stabilize the magnetic field as discussed above and in ref. [37]. The resonance condition ('excited-state energy') of the matter-wave emitters is determined by the detuning of the hyperfine spin and the zero point shifts to both states induced by the state-selective potential. Because we can currently control the wavelength only to an accuracy of 0.02 nm r.m.s., the overall uncertainty is limited to a maximum of ±340 Hz r.m.s., with the most extreme fluctuations limited to 1 kHz. To address and monitor this issue, we bracket each measurement (such as measuring the time evolution at a given detuning) by a resonance curve; an average of such resonance curves is shown in Extended Data Fig. 1 (see also figure 5 in ref. [37]). The resonance curve is taken without any transverse lattices on, with a low atom number in the optical trap (around 30,000 atoms) and only at partial transfer (at most 30%) to minimize systematic mean-field and density shifts. The residual systematic shift of the resonance condition due to mean-field and density effects is estimated to be less than 100 Hz by using direct simulation of resonance curves with the one-dimensional time-dependent Gross–Pitaevskii equation. The scatter of the centre of the resonance curves during a typical measurement has an r.m.s. value of 0.3 kHz, which is the quoted uncertainty of the detuning and also matches the expected wavelength reproducibility of 0.02 nm.

To characterize inhomogeneities of the state-selective optical potential, first we precisely calibrate the Rabi coupling strength (for a range of coupling strengths) in the absence of state-selective potentials. We then compare the maximum observed population transfer in a Rabi spectrum to the expected maximum population transfer into the lattice. Based on the comparison, we estimate an upper bound for the inhomogeneity of 300 Hz r.m.s. We note that the inhomogeneities of the trapping potential at 1,064 nm do not exceed 20 Hz r.m.s. across the sample. For comparison, the absolute magnitude of the spectroscopic shift of $|1, -1\rangle \leftrightarrow |2, 0\rangle$ in the centre of the optical trap does not exceed 400 Hz.

Background subtraction. The sequence used to thin out the atomic sample leaves roughly 10^3 atoms in the $|b\rangle$ state before the microwave pulse is applied. This results in a diffuse background in the momentum distributions, as illustrated in Extended Data Fig. 2. We remove this background by subtracting reference data taken for zero pulse time. The result is shown in Fig. 2c.

In Fig. 3f we also show the subtraction of background due to the very small fraction of higher-band population. The first excited band is expected at approximately $2\pi \times 36(1)$ kHz or $\pm 3\hbar k_r$. For the subtraction, we first fit three Gaussian peaks to the adiabatic ramp and one soft-edge box and two Gaussians to the sudden turn-on data, requiring identical atom numbers in the soft-edge box and the small Gaussian. The fitted functions are subtracted from the data, which then yield the main plot in Fig. 3f. The number of atoms emitted from higher bands is of the order of 510(30) for the sudden turn-on and 260(30) for the adiabatic ramp, which is less than 1 atom in a higher band per tube. The total number of atoms emitted

from higher bands changes with the pulse area because spurious emission from the higher bands is in the Markovian regime.

Energy-shift data. The main motivation for the precise momentum calibration described above lies in the small size of the energy shift. Another challenge is the blurring of the distribution due to propagation effects for small coupling strengths (that is, long pulses). We use two measures for the determination of the energy of the emitted wavepackets: the squared separation of the wavepacket centres (extracted from the fit) and the second moment of the (centred) distribution. The accuracy of the peak-separation measure is limited by the fact that it ignores the physical broadening of the momentum distribution at larger coupling strengths and shorter times, whereas the second moment is sensitive to blurring of the wave-packets during detection. The data obtained using both methods are shown in Extended Data Fig. 3. In the non-Markovian regime, $\Omega/\Delta > 1$, the peaks become indistinguishable (see the apex of the parabola in Fig. 2c) and a meaningful measure of the shift cannot be extracted with either method.

Numerical simulation of array effects. As stated in the main text, the Hamiltonian of the multi-site array[4] predicts the (resonant) transfer of excitations between neighbouring emitters[5], in some similarity to the mechanisms for radiation trapping in an optically thick sample. Instead of attempting to solve this Hamiltonian, here we consider a simplistic model of an array of three emitters that is coupled to a quantized mode structure reflecting the weak longitudinal harmonic confinement. We chose our simplistic three-site model to have a centrally occupied site as the simplest spatially symmetric generalization of the isolated-emitter situation, which also corresponds to an 'average segment' in our system, with approximately one empty neighbour on each side of a populated site.

We start from the Rabi Hamiltonian (in the rotating-wave approximation) and expand it to couple one or several sites ($|r\rangle$) to many different, weakly confined levels ($|b\rangle$). This Hamiltonian is (for simplicity only shown for two sites, but readily expanded to n sites)

$$
\hat{H} = \frac{\hbar}{2}
\begin{bmatrix}
2\bar{\delta}_1 & 0 & \Omega\gamma_{1,1} & \Omega\gamma_{1,2} & \cdots \\
0 & 2\bar{\delta}_2 & \Omega\gamma_{2,1} & \Omega\gamma_{2,2} & \\
\Omega\gamma_{1,1} & \Omega\gamma_{2,1} & -2\Delta + \omega_z & 0 & \\
\Omega\gamma_{1,2} & \Omega\gamma_{2,2} & 0 & -2\Delta + 3\omega_z & \\
\vdots & & & & \ddots
\end{bmatrix}
$$

where $\bar{\delta}_i = m\omega_z^2 r_i^2/(2\hbar)$ is a site-dependent detuning (that is, a site-dependent offset due to the weak harmonic confinement ω_z experienced by both lattice-trapped and free atoms) and $\gamma_{i,j}$ represents overlaps between final- and initial-state wavefunctions (calculated numerically). We use modes up to a fixed frequency ($\omega_{max} = 2\pi \times 5\,\mathrm{kHz}$) and restrict ourselves to $\Delta + 2\Omega < \omega_{max}$.

The results of the simulation for the Markovian parameters discussed in the main text are shown in Extended Data Fig. 4a, b. The simulated decay for an iso-lated emitter reproduces the prediction of our analytical model[6]—small discrepan-cies arise from the fact that the latter neglects terms of order $(\Delta/\omega_0)^2$ and $(\Omega/\omega_0)^2$

and higher, whereas our numerical simulation retains all orders. For the three-site array, the presence of neighbouring wells leads to a slowdown of the decay. The origin of this behaviour is reabsorption of emitted population by initially empty neighbours, as seen in Extended Data Fig. 4b. For the array considered, the process also leads to the formation of a temporary plateau in the overall site population, which may be related to the offset observed in the experiment. However, we cau-tion that the long-time decay occurs in a regime not accessible experimentally (we assumed a denser mode structure to extend the continuum approximation; see below), and also the dynamics may be different in an optical lattice extending over the entire mode volume.

In Extended Data Fig. 4c we plot the dynamics in the extreme non-Markovian regime at the edge, where the coupling strength is much larger than the excited-state energy. In this case, we see that the single emitter displays oscillatory dynamics that quickly damps out and settles to a non-zero value, again in agreement with the analytical theory. On the other hand, the three-emitter array shows oscillatory dynamics of much greater amplitude and longer duration. We interpret this as a coherent enhancement of the dynamics through tunnelling to nearest neighbours. The range of this tunnelling diverges at the band edge, causing the marked differ-ence between single emitter and three emitters.

From our simulations we gain additional insight into the effects of the quan-tized mode structure. As discussed in the main text, the mode structure should act like a true continuum for short enough times, where uncertainty should 'wash out' the levels. The simulations provide a quantitative test for this. The simplest comparison is for an isolated emitter in the Markovian limit. We see that for early times, the Markovian prediction[6] quantitatively agrees with the numerical solution, with a marked deviation ('revival') observable only at $t^* > 0.25[\omega_z/(2\pi)]^{-1}$ (we restrict data taking to $t < t^* = 2.6\,\mathrm{ms}$ in the experiments, in all but one case.) This is independent of the set harmonic trapping frequency and the location of the site in the array (centre or off-centre). We note that similar results are also obtained if the continuum is discretized by assuming a periodic-box-type potential, where the revival time depends on the length of the box. We furthermore note that our simulation does not reproduce δ_L for long times.

Data availability. The data that support the findings of this study are available from the corresponding author upon reasonable request.

34. Pertot, D., Greif, D., Albert, S., Gadway, B. & Schneble, D. Versatile transporter apparatus for experiments with optically trapped Bose–Einstein condensates. *J. Phys. B* **42**, 215305 (2009).
35. Campbell, G. K. et al. Imaging the Mott insulator shells by using atomic clock shifts. *Science* **313**, 649–652 (2006).
36. Gadway, B., Pertot, D., Reimann, R., Cohen, M. G. & Schneble, D. Analysis of Kapitza–Dirac diffraction patterns beyond the Raman–Nath regime. *Opt. Express* **17**, 19173–19180 (2009).
37. Krinner, L., Stewart, M., Pazmiño, A. & Schneble, D. In situ magnetometry for experiments with atomic quantum gases. *Rev. Sci. Instrum.* **89**, 013108 (2018).
38. Deng, L. et al. Temporal, matter-wave-dispersion Talbot effect. *Phys. Rev. Lett.* **83**, 5407–5411 (1999).
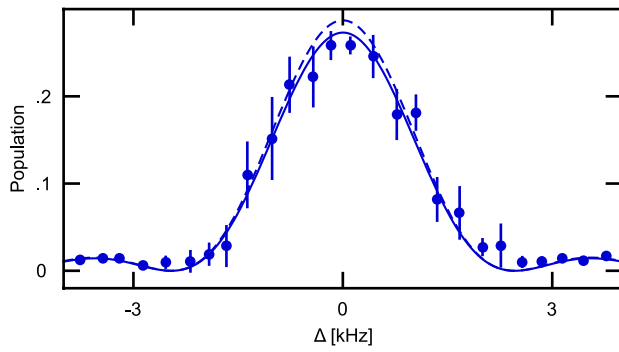
Extended Data Fig. 1 | Average spectrum of coupling stationary atoms into the z lattice. The spectrum was generated from a series of 17 spectra taken over a one-day period, whose fitted centres are shifted to zero. The coupling strength is $\Omega = 740(10)$ Hz and the pulse time is 400 μs, with the data points binned into 300-Hz-wide bins. The solid curve is a fit to the data with Ω as a free-fitting parameter and the dashed curve has no free parameters. The effective coupling strength was calculated using the wavefunction overlap between free and trapped species, $\gamma_0 = 0.72$.
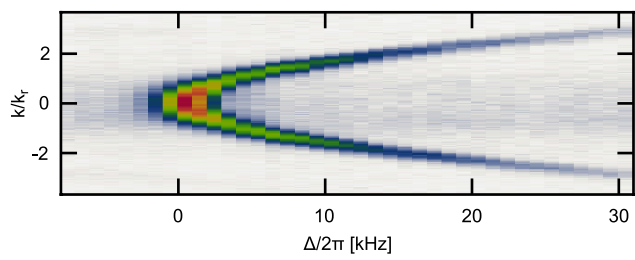
Extended Data Fig. 2 | Raw momentum spectrum. The spectrum shows a detuning-independent, diffuse background of roughly 10^3 atoms. The spectrum was acquired as described in the main text, Fig. 2 and Methods; colour scale is identical to Fig. 2c.
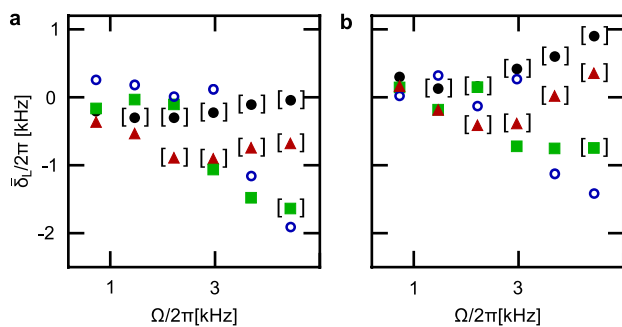
Extended Data Fig. 3 | Raw data used to obtain the energy shift.
a, **b**, Second moment of k (**a**) and half-separation squared (**b**) both
subtracted by $\Delta/(2\pi)$. The detuning $\Delta/(2\pi)$ is 1.0 kHz (black disks),
2.0 kHz (red triangles), 4.0 kHz (green squares) and 6.0 kHz (blue circles).
Points in brackets correspond to the non-Markovian regime, $\Omega/\Delta > 1$.
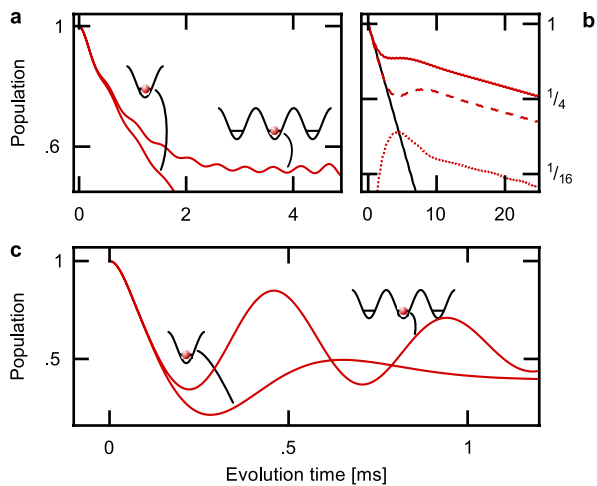
Extended Data Fig. 4 | Simulated decay dynamics for a 1-site and a 3-site model (with the central site initially populated). a, Dynamics of the two models, as depicted in the insets, for $\Delta = 2\pi \times 1.9$ kHz and $\Omega = 2\pi \times 0.74$ kHz, with $\omega_z = 2\pi \times 0.1$ kHz. **b,** Long-time decay dynamics of the 1-site (black) and 3-site (red) models for $\Omega = 2\pi \times 0.74$ kHz and $\Delta = 2\pi \times 1.9$ kHz, with $\omega_z = 2\pi \times 5$ Hz. The dashed red line shows the population of the central, initially populated, site; the dotted red line shows the population of the neighbouring sites. **c,** Dynamics of the two models for $\Delta = -2\pi \times 0.1$ kHz and $\Omega = 2\pi \times 3$ kHz, with $\omega_z = 2\pi \times 0.1$ kHz.